

# Surface reconstruction, doping and vacancy engineering to improve the overall water splitting of CoP nanoarrays

Yongkai Sun<sup>1</sup>, Wenyuan Sun<sup>2</sup>, Lihong Chen<sup>2</sup>, Alan Meng<sup>3</sup> (✉), Guicun Li<sup>2</sup>, Lei Wang<sup>3</sup>, Jianfeng Huang<sup>4</sup>, Aili Song<sup>5</sup>, Zhenhui Zhang<sup>2</sup>, and Zhenjiang Li<sup>2</sup> (✉)

<sup>1</sup> College of Electromechanical Engineering, Qingdao University of Science and Technology, Qingdao 266061, China

<sup>2</sup> College of Materials Science and Engineering, Qingdao University of Science and Technology, Qingdao 266042, China

<sup>3</sup> Key Laboratory of Optic-electric Sensing and Analytical Chemistry for Life Science MOE, College of Chemistry and Molecular Engineering, Qingdao University of Science and Technology, Qingdao 266042, China

<sup>4</sup> School of Material Science and Engineering, International S&T Cooperation Foundation of Shaanxi Province, Xi'an Key Laboratory of Green Manufacture of Ceramic Materials, Shaanxi University of Science and Technology, Xi'an 710021, China

<sup>5</sup> Qingdao Huanghai University, Qingdao 266000, China

© Tsinghua University Press 2022

Received: 18 April 2022 / Revised: 5 June 2022 / Accepted: 26 June 2022

## ABSTRACT

Development of a general regulatory strategy for efficient overall water splitting remains a challenging task. Herein, a simple, cost-fairness, and general fluorination strategy is developed to realize surface reconstruction, heteroatom doping, and vacancies engineering over cobalt phosphide (CoP) for acquiring high-performance bifunctional electrocatalysts. Specifically, the surface of CoP nanoarrays (NAs) becomes rougher, meanwhile F doped into CoP lattice and creating amounts of P vacancies by fluorination, which caused the increase of active sites and regulation of charge distribution, resulting the excellent electrocatalyst performance of F-CoP NAs/copper foam (CF). The optimized F-CoP NAs/CF delivers a lower overpotential of only 35 mV at 10 mA·cm<sup>-2</sup> for hydrogen evolution reaction (HER) and 231 mV at 50 mA·cm<sup>-2</sup> for oxygen evolution reaction (OER), and the corresponding overall water splitting requires only 1.48 V cell voltage at 10 mA·cm<sup>-2</sup>, which are superior to the most state-of-the-art reported electrocatalysts. This work provides an innovative and feasible strategy to construct efficient electrocatalysts.

## KEYWORDS

fluorination, surface reconstruction, F atom doping, P vacancies, overall water splitting

## 1 Introduction

The ever-growing demand for energy coupled with the environmental concerns associated with carbon dioxide emission has led to increased focus on the development of sustainable and clean energy sources [1–3]. Hydrogen has been regarded as ideal energy carrier to replace the conventional fossil fuels and alleviate the environmental problems thanks to its eco-friendliness and high energy density [4, 5]. The water splitting reaction provides a convenient way for hydrogen production, which includes two half reactions: hydrogen evolution reaction (HER) and oxygen evolution reaction (OER). Nevertheless, the energy conversion efficiencies are relatively low owing to the sluggish kinetic for HER and OER, which requires efficient electrocatalysts to expedite HER and OER process [6–8].

As the state-of-the-art electrocatalysts for water electrolysis, Pt/C and RuO<sub>2</sub> electrodes possess superior activity in HER and OER, respectively. However, noble-metal based catalysts are impractical for large-scale application owing to their scarcity, high cost, as well as the unsatisfactory durability [9, 10]. To realize the efficient and affordable water splitting, the earth-abundant electrocatalysts with low overpotential and rapid kinetics should be explored. The transition metal compounds have attracted considerable attention thanks to their low-cost, earth-abundance,

and excellent electrical conductivity [11], such as various transition metal sulfides [12], phosphides [13], nitrides [14], and selenides [15], etc. [16]. Among these reported electrocatalysts, transition metal phosphides (TMPs), especially cobalt-based phosphides, have been extensively investigated as promising electrocatalysts for HER and OER [17, 18]. However, the intrinsic activity and durability of pristine electrocatalytic materials are still far from satisfactory [19, 20].

Generally, the electrocatalytic activities extensively rely on the number of active sites and electronic structure of electrocatalyst. Thus, to obtain the satisfactory catalytic activity, the rational design for the electrocatalyst needs to be executed from the above two aspects. On the one hand, to achieve more active sites, morphology design is an effective strategy, where even a small refinement in morphology can improve the electrocatalytic performance over several folds [21, 22]. For example, Zhang et al., prepared a series of cobalt phosphide (CoP) electrocatalysts with nanosheets, nanowires, nanorods, and nanoblocks, the clustered CoP nanorods showing the best HER performance with only an overpotential of 71 mV at a current density of 10 mA·cm<sup>-2</sup>, and a low Tafel slope of 60.75 mV·dec<sup>-1</sup> in 1 M KOH [23]. In addition, in our earlier work, Co-P composites with different morphology were synthesized through adjusting the amount of phytic acid in the hydrothermal process. And the flower-like Co@CoP<sub>2</sub> shows

eminent electrocatalytic activity of HER with an overpotential of 55 mV and OER with an overpotential of 210 mV at a current density of  $10 \text{ mA}\cdot\text{cm}^{-2}$  in alkaline solution [24]. On the other hand, to further promote the catalytic activities of the electrocatalysts, diverse modification strategies have been explored to optimize the electronic structure, such as heteroatom doping, vacancy engineering, interface engineering, and phase engineering, etc. [25, 26]. Heteroatom doping has been widely considered as an efficient approach to turn the electronic structures, increase the polarity, and generate the new active phase, boosting the electrocatalytic performance [27, 28]. Lee et al., synthesized S-doped CoP electrocatalyst with highly activity and stability for water-splitting, and the excellent performance is related to the improved charge-transfer characteristics of the S:CoP NPs owing to the modifications induced in their electronic structure because of S-doping [29]. Luo et al., reported the synthesis of nitrogen-doped CoP nanoflowers supported on the conductive carbon cloth (N-CoP/CC), which exhibited a superior catalytic performances toward HER in a wide pH values. Especially, the overpotential at  $10 \text{ mA}\cdot\text{cm}^{-2}$  decreases from 79 to 25 mV after N doping under acidic conditions [30]. In addition, vacancy engineering has been studied intensively in water splitting electrocatalysts for enhanced electrocatalytic performances. Vacancies not only provide additional active sites but also adjust the electronic state of electrocatalyst and improve their conductivity, thus tailoring the intrinsic properties of catalysts [31]. Song et al., developed efficient  $\alpha\text{-Ni(OH)}_2$  electrocatalysts with controllable nickel vacancy concentrations. The reconstruction of the electronic structures can be promoted with the increase of  $V_{\text{Ni}}$  concentration to generate true active components, thereby boosting activities for both OER and urea oxidation reaction (UOR) [32]. Ding et al., constructed phosphorus vacancies in cobalt phosphide integrated with reduced graphene oxide (R-CoPx/rGO) as an efficient water oxidation electrocatalyst due to the fact that phosphorus vacancies can optimize the density of states (DOS) of the catalyst [33].

Given the above-mentioned analysis, morphology regulation, heteroatom doping, and vacancies engineering are the highly promising idea to improve the catalytic performance of electrocatalysts. However, it has not yet been reported to simultaneously achieve the surface reconstruction, F atom doping and P vacancies by a facile, cost-effective, and general strategy as well as systematic study the synergistic effect of multiple regulatory engineering on efficient overall water splitting.

Herein, the surface reconstruction, F atom doping, and P vacancies of CoP nanoarrays *in-situ* grown on copper foam (F-CoP NAs/CF) were realized simultaneously by a facile, cost-effective, and general molten fluorination method. Wherein, the surface reconstruction caused by fluorination results in a large number of concaves on the surface of the catalyst, increasing the number of active sites. Meanwhile, F doping into CoP lattice and generated a large number of P vacancies, optimizing the charge distribution. Based on the synergistic effect of above factors, the optimized F-CoP NAs/CF shows excellent electrocatalytic performance and stability, which are comparable to the commercial Pt/C or RuO<sub>2</sub> catalysts and superior to most of reported advanced electrocatalysts to date. This work provides an inspiration for the design and construction of overall water splitting electrocatalysts with excellent electrocatalytic performance and durability.

## 2 Experimental

### 2.1 Chemicals and materials

Cobalt nitrate hexahydrate ( $\text{Co}(\text{NO}_3)_2\cdot6\text{H}_2\text{O}$ ), ammonium fluoride ( $\text{NH}_4\text{F}$ ), urea ( $\text{CH}_4\text{N}_2\text{O}$ ), absolute ethylalcohol ( $\text{C}_2\text{H}_5\text{OH}$ ), and potassium hydroxide (KOH) were purchased from Sinopharm Chemical Reagent Co., Ltd. China. Nafion solution (5%) was obtained from Sigma-Aldrich (Shanghai, China). Commercial 20% Pt/C was purchased from Shanghai Hesen Electric Co., Ltd. (Shanghai, China). RuO<sub>2</sub> (99.9% metals basis) was purchased from Aladdin Co., USA. Copper foam (thickness:1.5 mm) was obtained from Shanxi LiYuan battery material Co., Ltd. All reagents were used as received without any purification.

( $\text{C}_2\text{H}_5\text{OH}$ ), and potassium hydroxide (KOH) were purchased from Sinopharm Chemical Reagent Co., Ltd. China. Nafion solution (5%) was obtained from Sigma-Aldrich (Shanghai, China). Commercial 20% Pt/C was purchased from Shanghai Hesen Electric Co., Ltd. (Shanghai, China). RuO<sub>2</sub> (99.9% metals basis) was purchased from Aladdin Co., USA. Copper foam (thickness:1.5 mm) was obtained from Shanxi LiYuan battery material Co., Ltd. All reagents were used as received without any purification.

### 2.1.1 Pre-treatment of CF

Commercial CF was first cut to  $1 \text{ cm} \times 1 \text{ cm}$  pieces. They were, then, immersed in HCl solution (3 M) under ultrasonic for 20 min, followed by washing with deionized (DI) water and anhydrous alcohol to remove the oxides and impurities from the CF pieces.

### 2.1.2 Synthesis of Co(OH)F NAs/CF

Typically, 0.5820 g  $\text{Co}(\text{NO}_3)_2\cdot6\text{H}_2\text{O}$ , 0.3704 g  $\text{NH}_4\text{F}$ , and 0.6006 g  $\text{CH}_4\text{N}_2\text{O}$  were dispersed into 20 mL DI water with continuous stirring for 10 min, and a light pink solution was obtained. Afterwards, a piece of CF ( $1 \text{ cm} \times 1 \text{ cm}$ ) was immersed into the above solution, then transferred into a Teflonlined stainless-steel autoclave and kept at 120 °C for 8 h. The Co(OH)F NAs/CF was obtained by washing with DI water and drying in vacuum at 60 °C.

### 2.1.3 Synthesis of CoP NAs/CF

To prepare CoP NAs/CF, the as-obtained sample Co(OH)F NAs/CF and  $\text{NaH}_2\text{PO}_2$  were placed in two separate porcelain boats.  $\text{NaH}_2\text{PO}_2$  was on the upstream, Co(OH)F NAs/CF was on the downstream, then, the quartz tube was calcined at 300 °C with a heating rate of  $2 \text{ }^{\circ}\text{C}\cdot\text{min}^{-1}$  and maintained for 2 h in an Ar flow atmosphere. With natural cooling, the sample was achieved, denoted as CoP NAs/CF.

### 2.1.4 Synthesis of the F-CoP NAs/CF

The molten salt fluorination process was performed to prepare F-CoP NAs/CF. Normally, 2 g of  $\text{NH}_4\text{F}$  in a glass bottle (10 mL) was heated to 250 °C for a certain time until melting. The as-prepared CoP NAs/CF was submerged into the molten ammonium fluoride for 60 s, and the products were removed and washed with DI water for several times, denoted as F-CoP NAs/CF. As a comparison, the F-CoP NAs/CF-30 electrocatalyst was obtained by shortening the fluorination time to 30 s. Meanwhile, the fluorination time was extended to 90 s to obtain the F-CoP/CF-90 electrocatalyst. The mass loading of fluorinated samples was  $1 \pm 0.1 \text{ mg}\cdot\text{cm}^{-2}$ , determined by weighing the CF before and after growing active materials.

## 2.2 Materials characterizations

The morphologies of the products were observed with scanning electron microscopy (SEM) images of an accelerated voltage of 5 kV using JSM-6460LV SEM and transmission electron microscopy (TEM) (H-7650, Hitachi Co., Japan), using an electron kinetic energy of 100 kV. To analysis the phase composition, X-ray diffraction (XRD) patterns for products were carried out on a Philips X'Pert Pro Super diffractometer with graphite-monochromatized Cu-K $\alpha$  radiation ( $\lambda = 1.541874 \text{ \AA}$ ) (Rigaku TTR-III, PHLIPS Co., the Netherlands). X-ray photoelectron spectroscopy (XPS) (ESCALAB250, Thermo Fisher Inc., USA) was used to determine the chemical compositions and the valence states of constituent elements. Electron paramagnetic resonance (EPR) spectra were recorded from a Bruker A 300 at 77 K.

### 2.3 Electrochemical measurements

The electrochemical measurements were carried out with a CHI760E electrochemical workstation (Chenhua Corp., Shanghai) using a standard three-electrode system in 1 M KOH electrolyte. Hg/HgO electrode and platinum electrode served as the reference electrode and the counter electrode respectively, and the copper foam loaded with active materials was directly used as the working electrode. All data in electrochemical measurements were reported with iR compensation. For comparison, Pt/C/CF (20 wt.%, loaded on copper foam with  $\sim 1 \text{ mg}\cdot\text{cm}^{-2}$ ) was prepared for HER measurement. Meanwhile, RuO<sub>2</sub>/CF (loaded on copper foam with  $\sim 1 \text{ mg}\cdot\text{cm}^{-2}$ ) was also prepared for OER measurement. The overall watersplitting measurement was carried out in a standard two-electrode system using F-CoP NAs/CF as the cathode and anode in 1 M KOH electrolyte. The electrochemical surface area (ECSA) was obtained from the  $C_{dl}$  by collecting CVs at various scan rates of 10, 20, 30, 40, and 50 mV·s<sup>-1</sup> in the non-Faradaic region. The electrochemical impedance spectroscopy (EIS) was conducted in the Faradaic region to estimate the charge-transfer resistance ( $R_{ct}$ ). All the relative data were reported versus reversible hydrogen electrode (RHE) potentials according to the following Eq. (1)

$$E_{\text{RHE}} = E_{\text{Hg/HgO}} + 0.0591 \times \text{pH} + 0.098 \quad (1)$$

### 2.4 Density functional theory (DFT) calculations

The DFT computations were carried out by Vienna *ab initio* simulation package (VASP) using the projector augmented wave (PAW) method [34]. The exchange correlation potential was represented by the Perdew–Burke–Ernzerhof (PBE) functional within the generalized gradient approximation (GGA) [35]. The computational model in this paper used a CoP (211) surface with eight atomic layers. In the F-CoP (211) surface system, F atoms replaced part of P atoms, and the P vacancy would be formed on the surface. The cutoff energy for the plane-wave-basis was set to be 500 eV, and the convergence tolerances of energy and force were set to  $1.0 \times 10^{-5} \text{ eV}\cdot\text{atom}^{-1}$  and  $10^{-3} \text{ eV}\cdot\text{\AA}^{-1}$ , respectively. The k-point sampling grid was set to  $5 \times 5 \times 1$ . The vacuum layer was set to 15 Å. During structural optimizations, the bottom four layers atoms of CoP (211) surface were fixed. The Gibbs free energy change ( $\Delta G$ ) of the elementary step of the hydrogen evolution reaction was calculated by Eq. (2)

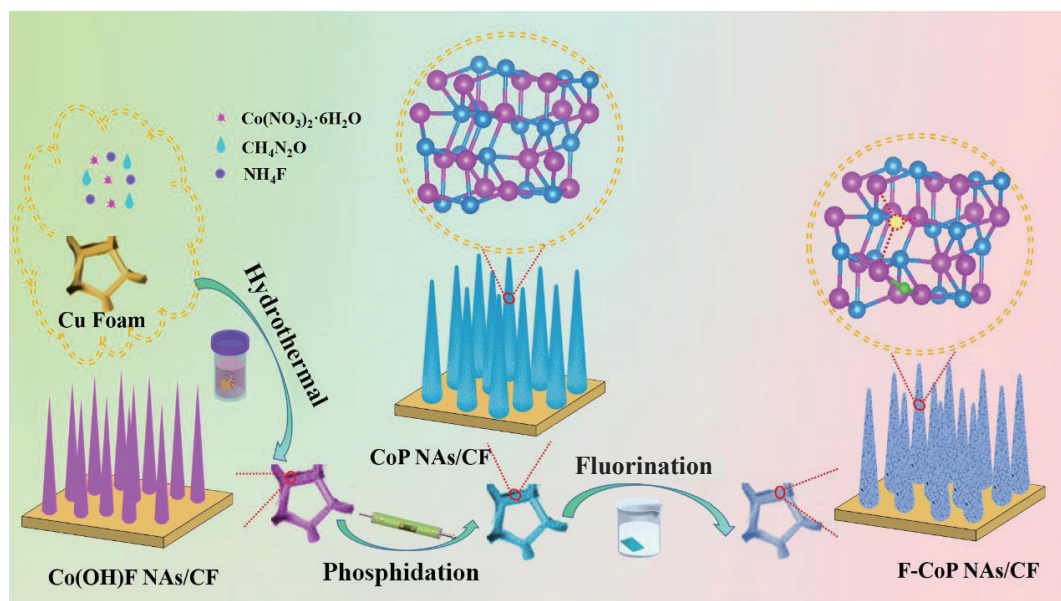
$$\Delta G = \Delta E + \Delta E_{\text{ZPE}} - T\Delta S \quad (2)$$

where  $\Delta E$  is the total energy difference,  $\Delta E_{\text{ZPE}}$  is the change in the zero-point energy and the entropy,  $T$  is the temperature ( $T = 298.15 \text{ K}$ ), and  $\Delta S$  is the entropy change.

## 3 Results and discussion

The low-cost CF with superhigh electrical conductivity and three-dimensional (3D) macroporous feature was utilized as a supporting substrate for distributing the catalysts. As presented in Scheme 1, a piece of treated CF was immersed in a mixed solution containing  $\text{Co}(\text{NO}_3)_2\cdot 6\text{H}_2\text{O}$ ,  $\text{NH}_4\text{F}$ , and  $\text{CH}_4\text{N}_2\text{O}$ . The  $\text{Co(OH)}\text{F}$  with uniform size acicular nanoarrays was directly grown on CF through a gentle hydrothermal method (as shown in Fig. S1 in the Electronic Supplementary Material (ESM)). In the next step, the as-prepared  $\text{Co(OH)}\text{F}$  NAs/CF was phosphorized to CoP NAs/CF through calcination in Ar atmosphere. Finally, the F-CoP NAs/CF was obtained via fluorinated the CoP NAs/CF in  $\text{NH}_4\text{F}$  molten salt for only 60 s. Fluorination not only results in dramatic surface reconstruction of catalyst, but also leads to F atom doping and P vacancies forming. The micromorphology and nanostructure of various samples before and after fluorination for different time were shown in SEM and TEM images.

As shown in Fig. 1(a), after phosphorization, the micromorphology of CoP NAs grown on CF substrate is similar to that of precursor and the surface is relatively smooth (Fig. 1(b)). The energy dispersive spectroscopy (EDS) image (the inset of Fig. 1(b)) revealed that the materials after phosphorization are composed of Cu, Co, and P. And the corresponding TEM image of CoP NAs/CF was carried out (Fig. 1(c)). It can be seen that a relatively smooth surface of CoP can be further verified. After fluorination, F-CoP NAs/CF maintains uniformly morphology and the highly ordered nanoarrays structures similar to the micromorphology of CoP NAs/CF (Fig. 1(d)). Whereas the surface morphology of the electrocatalysts has changed significantly, the smooth surface of the nanoarrays became quite rough, and possessed amounts of concaves (Fig. 1(e)). The EDS analysis (the inset of Fig. 1(e)) suggests that the as-prepared material is consisted of Cu, Co, P, and F, speculating that F-CoP NAs/CF was successfully synthesized. The corresponding TEM image further proved the results of SEM images (Fig. 1(f)). Besides, compared with F-CoP



**Scheme 1** Schematic illustration of the preparation of F-CoP NAs/CF electrode.

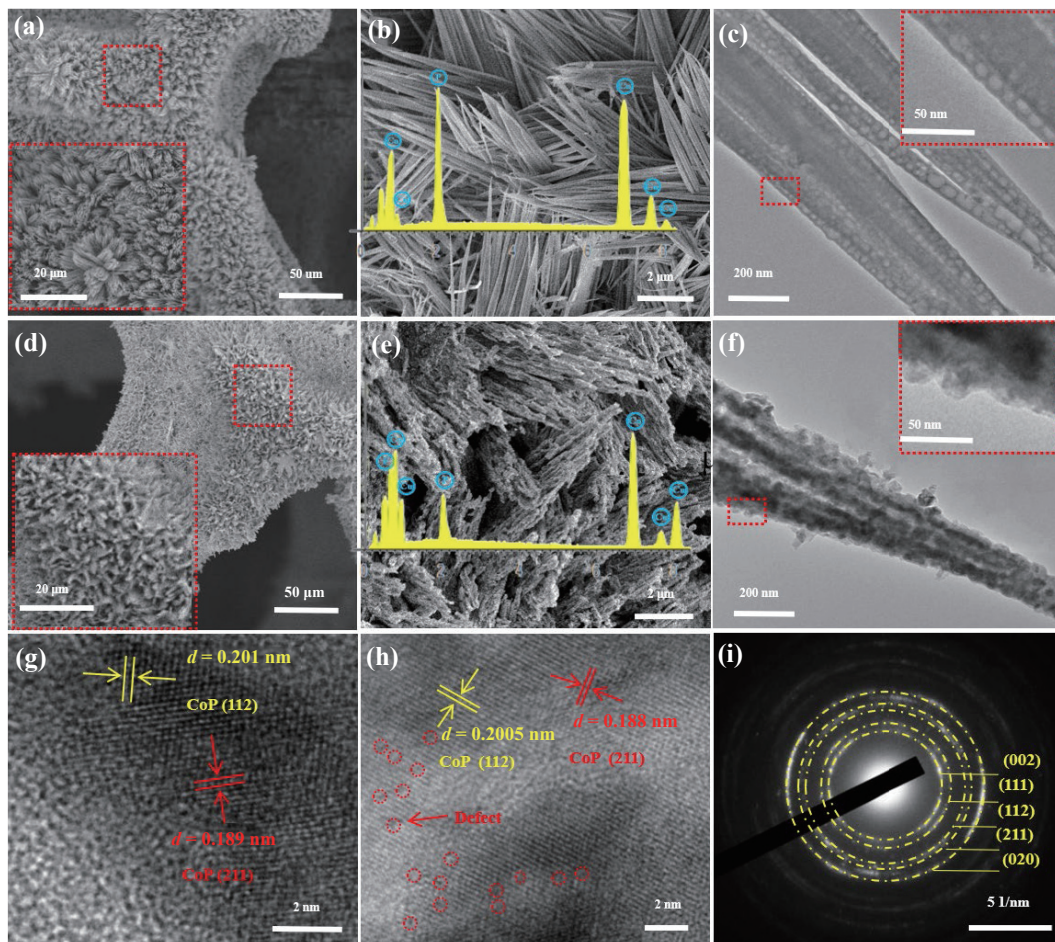


**Figure 1** (a) and (b) SEM and (c) TEM images of CoP NAs/CF. (d) and (e) SEM and (f) TEM images of F-CoP NAs/CF. HRTEM of (g) CoP NAs/CF and (h) F-CoP NAs/CF. (i) The selected area electron diffraction measurement of F-CoP NAs/CF.

NAs/CF, F-CoP NAs/CF-30 also maintains the ordered nanoarrays structures, but the surface morphology of the electrocatalyst showed less roughness (Figs. S2(a)–S2(c) in the ESM). For F-CoP/CF-90, the ordered nanoarrays structure was collapsed completely (Figs. S2(d)–S2(f) in the ESM). Taken together, F-CoP NAs/CF has the most appropriate surface reconstruction on the basis of keeping an ordered nanoarrays. Such a structure is highly desired as it can provide highly exposed and easily accessible active sites for the electrocatalytic reaction. In addition, the high-resolution TEM (HRTEM) images of CoP NAs/CF (Fig. 1(g)) showed two kinds of obvious lattice fringes with interspaces of about 0.189 and 0.201 nm, corresponding to the (211) and (112) planes of CoP, respectively. And the interspaces of F-CoP NAs/CF are 0.188 and 0.2005 nm, which are basically consistent with the interspaces of CoP NAs/CF (Fig. 1(h)), indicating that fluorination does not alter the crystal phase of CoP. Moreover, some visible discontinuous lattice fringes were observed in the red circles, indicating the presence of defects, which may be caused by the P vacancies in the F-CoP NAs/CF. As shown in Fig. 1(i), the selected area electron diffraction (SAED) measurement of F-CoP NAs/CF also shows all the diffraction rings match well with standard CoP.

The crystal phase structure of the CoP NAs/CF and F-CoP NAs/CF was confirmed by XRD pattern. As shown in Fig. 2(a), all characteristic diffraction peaks of both F-CoP NAs/CF and CoP NAs/CF electrocatalysts are well indexed to orthorhombic CoP (JCPDS 20-0497) except three diffraction peaks of CF substrate (Cu, JCPDS 04-0836), which is consistent with SAED results, and no peaks indexed to fluorine species can be detected. However, EDS analysis confirms the presence of F in sample, inferring that the F

was doped into CoP lattice. Interestingly, the characteristic peaks intensity of F-CoP NAs/CF decreases comparing with CoP NAs/CF (when normalized their CF peaks intensity), which may be due to the increase of lattice defects caused by F atom doping. The EPR spectra were shown in Fig. 2(b), compared with the CoP NAs/CF electrocatalyst, F-CoP NAs/CF possessed a fairly high symmetric signal at  $g \approx 2.003$ , which ascribes to the appearance of unpaired electrons in the F-CoP NAs/CF, further suggesting the F atom doping accompanied with the formation of P vacancies in the F-CoP NAs/CF electrocatalyst. The reason for the generation of P vacancies could be explained as below: When F doping in CoP lattice, F replaced the position of P, and the F-Co bond formed, leading to the broken of the initial P-Co bonds, which is conducive to the generation of isolated P, and then isolated P escaped to induce the P vacancies forming. To realize the surface electronic state of CoP NAs/CF and F-CoP NAs/CF, the XPS result was investigated. The full XPS survey spectra were shown in Fig. 2(c), besides the signals of Co, P, and Cu elements, the new signal of F element appeared in the XPS pattern of F-CoP NAs/CF in comparison with CoP NAs/CF, indicating the presence of F in F-CoP NAs/CF. And the corresponding atomic percentage of each element in F-CoP NAs/CF was shown in Table S1 in the ESM. In F 1s XPS spectra (Fig. 2(d)), the F-CoP NAs/CF displays a characteristic peak at 685.1 eV attributed to the F-Co bonds [36], indicating F was successfully doped into CoP lattice by replacing P site. Figure 2(e) shows the Co 2p high-resolution region spectra. For F-CoP NAs/CF, the two main peaks situated at 778.8 and 782.9 eV are associated with Co 2p<sub>3/2</sub>, and additional two main peaks located at 793.6 and 798.8 eV are attributed to Co 2p<sub>1/2</sub>. In addition, the two peaks appearing 788.2 and 804.7 eV are

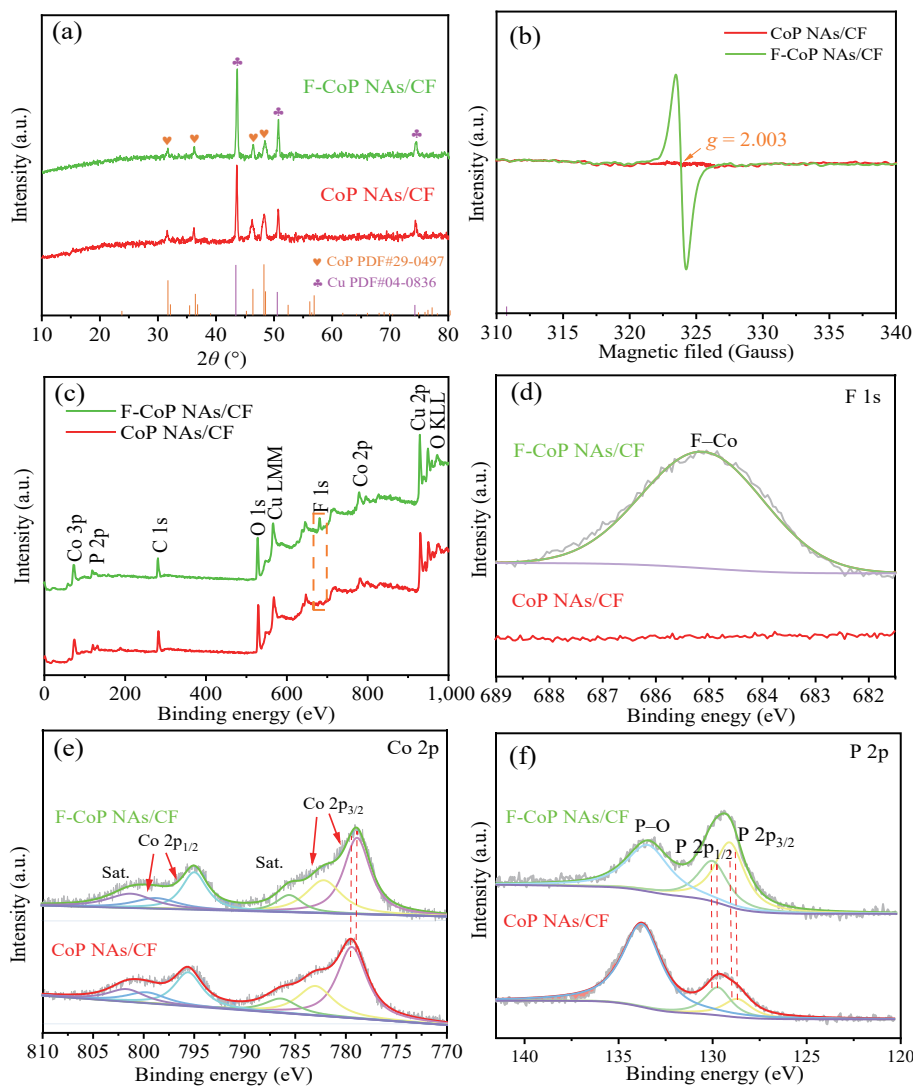


**Figure 2** (a) XRD patterns and (b) EPR spectra and XPS results of F-CoP NAs/CF and CoP NAs/CF: (c) full survey scan, (d) F 1s, (e) Co 2p, and (f) P 2p.

assigned to the shakeup satellite peaks of Co 2p. Especially to deserve to be mentioned, compared with bare CoP NAs/CF, the binding energy is down-shifted by  $\sim 0.5$  eV in F-CoP NAs/CF. It implies that the oxidation state of Co increases slightly in CoP due to the presence of the P vacancies [37]. In addition, the P 2p high-resolution region spectrum of F-CoP/CF has two peaks corresponding to Co-P bonds at 129.1 and 130.2 eV for P 2p<sub>3/2</sub> and P 2p<sub>1/2</sub>, respectively, and the broad peak at 133.7 eV is associated with the phosphates (Fig. 2(f)), arising from air contact. It is important to note that the P 2p in F-CoP NAs/CF is positively shifted ( $\approx 0.4$  eV) compared with bare CoP NAs/CF, suggesting P partially loses charges as compared to pristine CoP NAs/CF, which is ascribed to the stronger electronegativity of F than P. The above results indicated that F atom doping and P vacancies could change the electron structure, which is beneficial to improve the catalytic performance of the electrocatalyst [38].

The HER properties of as-prepared samples were examined through a standard three-electrode system in 1.0 M KOH. Figure 3(a) shows the HER polarization curves of CoP NAs/CF, F-CoP NAs/CF-30, F-CoP NAs/CF, F-CoP/CF-90, and Pt/C/CF. The F-CoP NAs/CF shows a very small overpotential of 35 mV at a current density of 10 mA·cm<sup>-2</sup>, which is superior to the Pt/C/CF (38 mV) benchmark at the same current density. Overpotentials of 42, 66, and 93 mV are needed to conduct a current density of 10 mA·cm<sup>-2</sup> for F-CoP/CF-90, F-CoP NAs/CF-30, and CoP NAs/CF, demonstrating the significant improvement of

fluorination in the HER activities. To investigate the HER kinetics of the corresponding catalysts, Tafel plots originated from the polarization curves were shown in Fig. 3(b). Tafel slope is 32 mV·dec<sup>-1</sup> for F-CoP NAs/CF, which is even smaller than that of Pt/C/CF (37 mV·dec<sup>-1</sup>). Such a small Tafel slope value fully confirms the fast kinetics of F-CoP NAs/CF, which further implies the excellent catalytic performance of the electrocatalyst. For comparison, the histograms of the overpotentials at 10 mA·cm<sup>-2</sup> and the Tafel slopes for CoP NAs/CF, F-CoP NAs/CF-30, F-CoP NAs/CF, F-CoP/CF-90, and Pt/C/CF are shown in Fig. 3(c), it clearly suggests the Pt-like HER activity of F-CoP NAs/CF, and the HER performance of F-CoP NAs/CF are very competitive to most recently reported catalysts shown in Fig. 3(e) and Table S2 in the ESM. Besides catalytic activity, electrocatalytic stability is another crucial criterion for practical application. As demonstrated in Fig. 3(d), the long-term stabilities of overpotential of 35 and 38 mV are obtained for F-CoP NAs/CF and Pt/C/CF, respectively. Obviously, the current density of the F-CoP NAs/CF electrode oscillates slightly and there is no significant current loss within 100 h.

In addition, the OER properties of F-CoP NAs/CF-30, F-CoP NAs/CF, F-CoP/CF-90, CoP NAs/CF, and RuO<sub>2</sub>/CF were also assessed. As shown in Fig. 4(a), F-CoP NAs/CF requires a very small overpotential of 231 mV to afford the current density of 50 mA·cm<sup>-2</sup>, which is much smaller than those of F-CoP NAs/CF-30 ( $\eta_{50} = 320$  mV), F-CoP/CF-90 ( $\eta_{50} = 304$  mV), CoP NAs/CF ( $\eta_{50} = 378$  mV), and RuO<sub>2</sub>/CF ( $\eta_{50} = 507$  mV). The results suggest

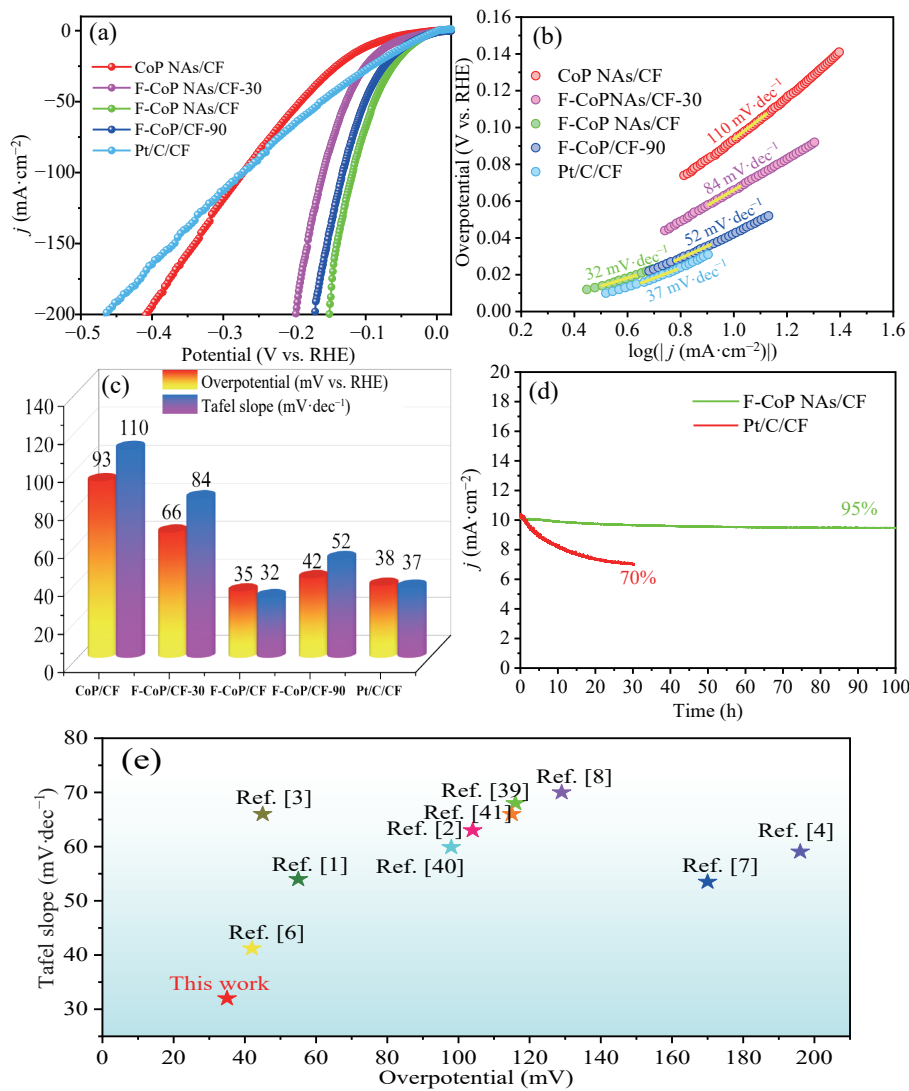


**Figure 3** (a) Polarization curves for HER, (b) the corresponding Tafel plots, and (c) comparison of overpotentials and Tafel slopes for CoP NAs/CF, F-CoP NAs/CF-30, F-CoP NAs/CF, F-CoP/CF-90, and Pt/C/CF. (d) Long-term stabilities of F-CoP NAs/CF and Pt/C/CF at the overpotential of 35 and 38 mV (vs. RHE), respectively, in 1 M KOH electrolyte. (e) Tafel slopes and overpotentials of F-CoP NAs/CF compared with those of the recently reported HER catalysts.

that F-CoP NAs/CF is an excellent OER catalyst in 1 M KOH. The F-CoP NAs/CF catalyst shows superior performance to RuO<sub>2</sub>/CF and many other state-of-the-art nonprecious-metal electrocatalysts (shown in Fig. 4(e) and Table S3 in the ESM). Figure 4(b) summarizes the Tafel slopes of the as-prepared electrodes. Compared with the values of 128.71 mV·dec<sup>-1</sup> for F-CoP NAs/CF-30, 91.55 mV·dec<sup>-1</sup> for F-CoP/CF-90, 147.25 mV·dec<sup>-1</sup> for CoP NAs/CF, and 135.42 mV·dec<sup>-1</sup> for RuO<sub>2</sub>/CF, F-CoP NAs/CF displays the lowest value of 73.19 mV·dec<sup>-1</sup>, indicating the favorable reaction kinetics of the F-CoP NAs/CF catalyst toward OER. Figure 4(c) exhibits the overpotentials and Tafel slopes of the various catalysts in the form of a histogram, which intuitively indicates the excellent OER performance of F-CoP NAs/CF. The durabilities of both F-CoP NAs/CF and RuO<sub>2</sub>/CF were evaluated by chronoamperometry curves, as shown in Fig. 4(d), compared with starting point, the current density shows a slight change at a constant potentials after 100 h OER test, indicating the excellent stability of F-CoP NAs/CF catalysts for OER in 1 M KOH, which is the apparent advantage of F-CoP NAs/CF as a high-performance OER electrocatalyst.

To elucidate the origins of the remarkable HER and OER performance of F-CoP NAs/CF, a series of characterizations were performed. First, the morphology analysis showed that the fluorination could lead to the surface reconstruction, which is helpful to provide more active sites. To further confirm this claim,

the test of the double layer capacitance ( $C_{dl}$ ) was performed, which can be determined by measuring in a non-Faradaic region of CV curves (Fig. S3 in the ESM), as shown in Fig. 5(a). And the  $C_{dl}$  of the F-CoP NAs/CF electrode was measured to be 91.2 mF·cm<sup>-2</sup>, which is larger than those of F-CoP NAs/CF-30 (47.7 mF·cm<sup>-2</sup>), F-CoP/CF-90 (52.9 mF·cm<sup>-2</sup>), and CoP NAs/CF (38.9 mF·cm<sup>-2</sup>). To better compare the activity of different electrocatalysts at an intrinsic level, ECSA pattern was drawn. As shown in Fig. S4 in the ESM, F-CoP NAs/CF possessed a greatest ECSA of 2,280 cm<sup>2</sup>, which was much larger than those of CoP NAs/CF (972.5 cm<sup>2</sup>), F-CoP NAs/CF-30 (1,192.5 cm<sup>2</sup>), and F-CoP NAs/CF-90 (1,322.5 cm<sup>2</sup>), respectively, indicating more active sites were exposed for F-CoP NAs/CF, which results in higher electrochemical activity. Second, the results of multiple characterization showed that F atom doping and P vacancies caused by fluorination can change the electronic structure of CoP, which will improve the charge transfer rate, and further boost their electrocatalytic performance. The accelerated charge transfer is verified by the drastically reduced diameter of the semicircle at high-frequency region in EIS patterns. The F-CoP NAs/CF catalyst exhibits the lowest charge-transfer impedance  $R_{ct} = 2.016 \Omega$  than those of F-CoP NAs/CF-30 ( $R_{ct} = 3.447 \Omega$ ), F-CoP/CF-90 ( $R_{ct} = 2.226 \Omega$ ), and CoP NAs/CF ( $R_{ct} = 10.21 \Omega$ ) catalysts (Fig. 5(b)) (the detail shown in Table S4 in the ESM), suggesting the efficient charge transfer kinetics and the superior conductivity of

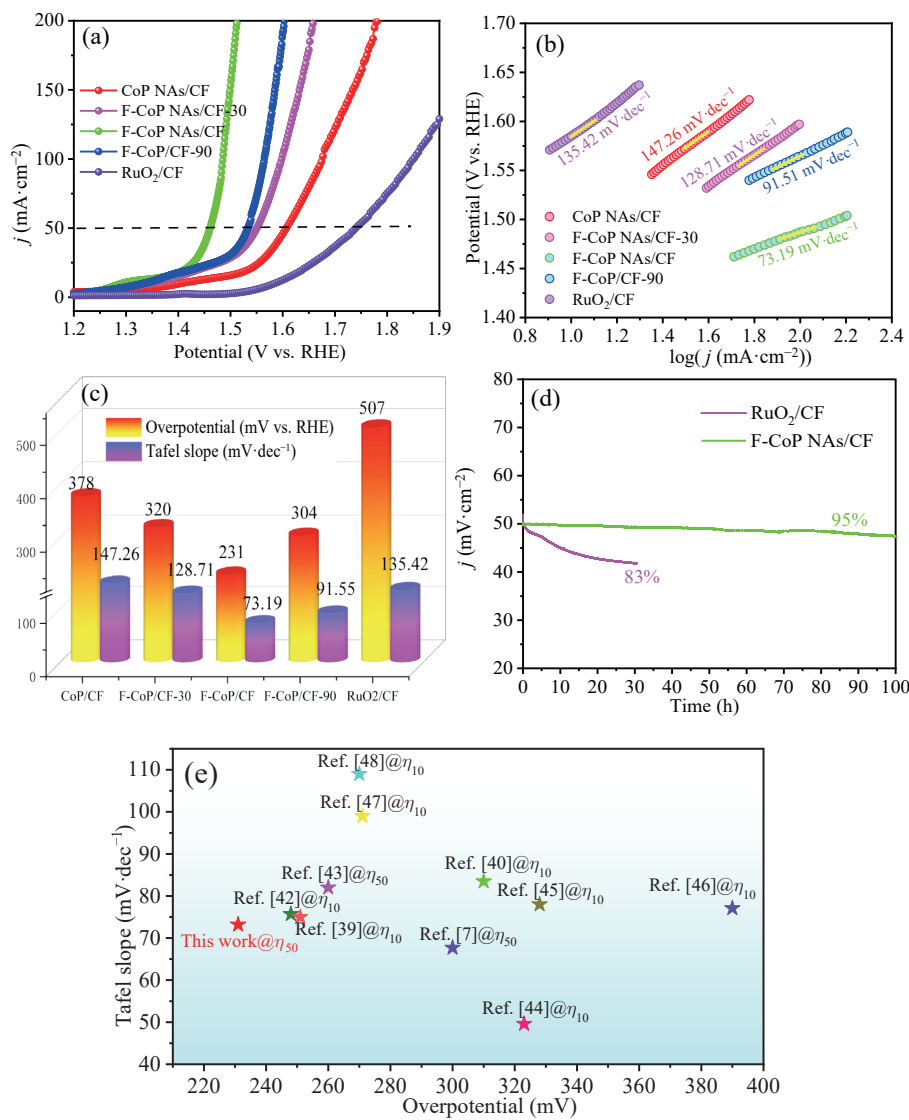


**Figure 4** (a) Polarization curves for OER and (b) the corresponding Tafel plots of different electrocatalysts in 1.0 M KOH solution. (c) Comparison of overpotentials and Tafel slopes for the different samples. (d) Long-term stabilities of F-CoP NAs/CF and RuO<sub>2</sub>/CF at the overpotential of 231 and 507 mV, respectively. (e) Tafel slopes and overpotentials of F-CoP NAs/CF compared with those of the state-of-the-art nonprecious-metal OER electrocatalysts.

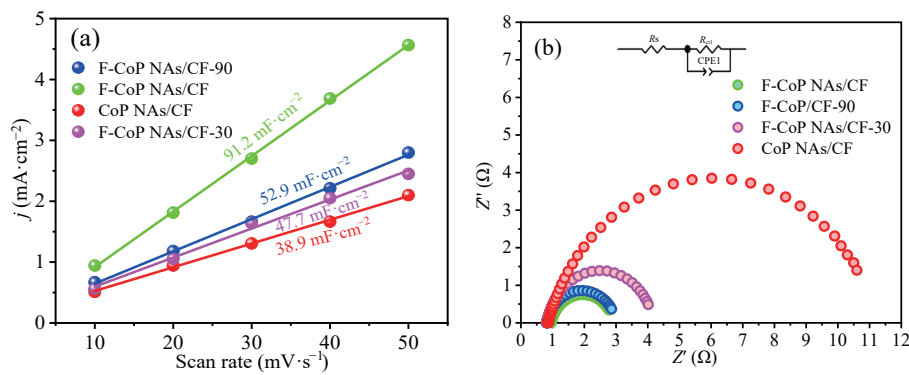


**Figure 5** (a) Capacitive current density plotted against the scan rates (10–50 mV·s<sup>-1</sup>) and (b) Nyquist plots of EIS of CoP NAs/CF, F-CoP NAs/CF-30, F-CoP NAs/CF, and F-CoP/CF-90 in 1 M KOH electrolyte.

the F-CoP NAs/CF compared to other catalysts, which will further improve the catalytic activity of the electrocatalysts.

To further understand the roles of the F atom doping and P vacancies on the electrocatalytic performance, the DFT computations were carried out. Firstly, the DOS and pDOS of d-band center of Co in CoP NAs/CF and F-CoP NAs/CF were analyzed. In general, DOS intensity at the Fermi level is intimately connected with the electrical conductivity of the materials [49].

Figures 6(a) and 6(b) show the atomic structure model of CoP NAs/CF and F-CoP NAs/CF, respectively, and the corresponding DOS of CoP and F-CoP are depicted in Figs. 6(c) and 6(d). DOS of F-CoP NAs/CF increased significantly, especially in the region near the Fermi level, the increased DOS indicated the rapid charge-transfer process, which is beneficial to accelerate the electrocatalytic reaction of the electrocatalyst. Notably, the d-band center (3d) of Co in CoP and F-CoP with respect to  $E_f$  was

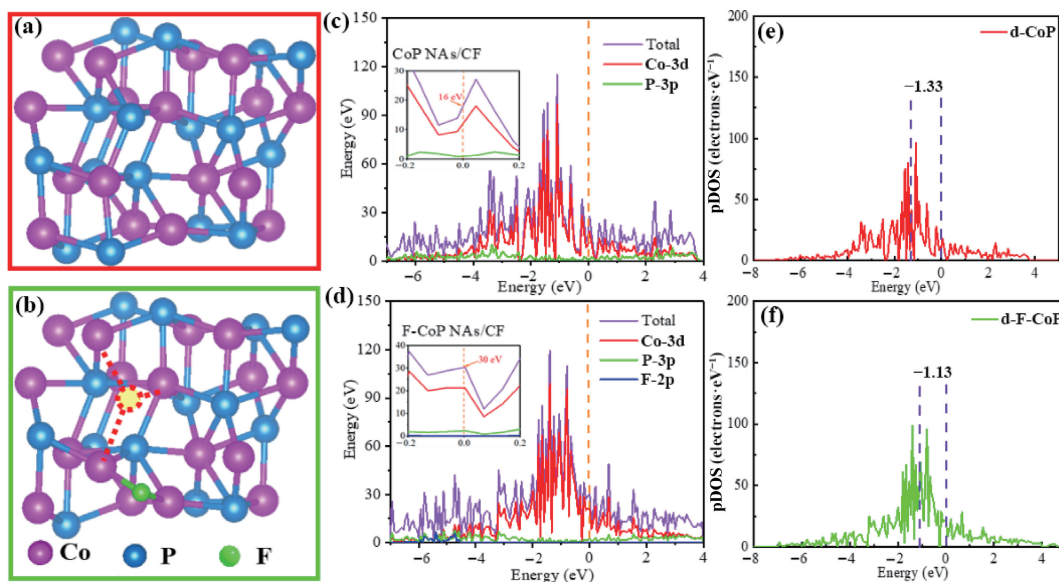


**Figure 6** The crystal structure of (a) CoP and (b) F-CoP, and blue, pink, and green spheres and red circle represent P, Co, and F atoms and vacancy, respectively. The corresponding DOS of (c) CoP and (d) F-CoP, and the pDOS of the d-state of Co in (e) CoP and (f) F-CoP, respectively.

calculated to be  $-1.33$  (Fig. 6(e)) and  $-1.13$  eV (Fig. 6(f)), respectively, manifesting that the d-band center of Co in CoP is shifted positively upon after fluorination. And the value of  $\varepsilon_d$  is calculated by Eq. (3)

$$\varepsilon_d = \frac{\int_{-\infty}^{\infty} x\rho(x) dx}{\int_{-\infty}^{\infty} \rho(x) dx}$$

where  $\varepsilon_d$  is the energy level of d states, and its value is the d band center, and the  $x$  and  $\rho(x)$  correspond to the abscissa and ordinate of Fig. 6(e), respectively [49]. The d-band center is useful to predict the adsorption behavior of small molecules on the surface of electrocatalyst [50]. Such a d-band center upshift could induce less electron filling in the antibonding states of F-CoP NAs/CF, which accounts for the strengthened OH<sup>-</sup> adsorption [51, 52], and then improve the OER performance of the electrocatalyst.

What's more, Figs. 7(a) and 7(c) show the charge difference distribution of CoP/CF and F-CoP/CF. Compared with CoP/CF, F sites and around the P vacancies are the electron-rich regions, and the electronic depletion is at the sites of Co in F-CoP/CF. From Figs. 7(b) and 7(d), the two-dimensional (2D) electronic location function displayed the variation of the charge distribution for CoP/CF before and after fluorination more intuitively. The charge accumulation at the F sites and around the P vacancies will favor H capture electron, thus further improve HER activity, which can be verified via the change of the hydrogen adsorption free energy ( $\Delta G_{H^*}$ ).  $\Delta G_{H^*}$  is utilized as a critical parameter in theoretically forecasting for HER activity of material. It was well-known that a corresponding  $\Delta G_{H^*}$  (close to  $\approx 0$  eV) can offer a respective HER activity with a small reaction barrier for an excellent electrocatalyst [53]. Therefore, to elucidate the change of  $\Delta G_{H^*}$  caused by the change of electronic structure due to fluorination,  $\Delta G_{H^*}$  values of the samples before and after fluorination were calculated. It can be seen from Fig. S5 in the ESM, the adsorption free energy of H on F-CoP (0.2 eV) showed better behavior than that in CoP ( $-0.35$  eV), indicating that the charge accumulation at the F sites and around the P vacancies caused by F fluorination can efficiently enhance HER performance. Similarly, the charge depletion at the Co sites will make OH more likely to lose electron, which facilitates OER process. Therefore, the optimization of charge distribution driven by the synergistic effect of F atom doping and P vacancies makes F-CoP NAs/CF a promising electrocatalyst for efficient overall water splitting.

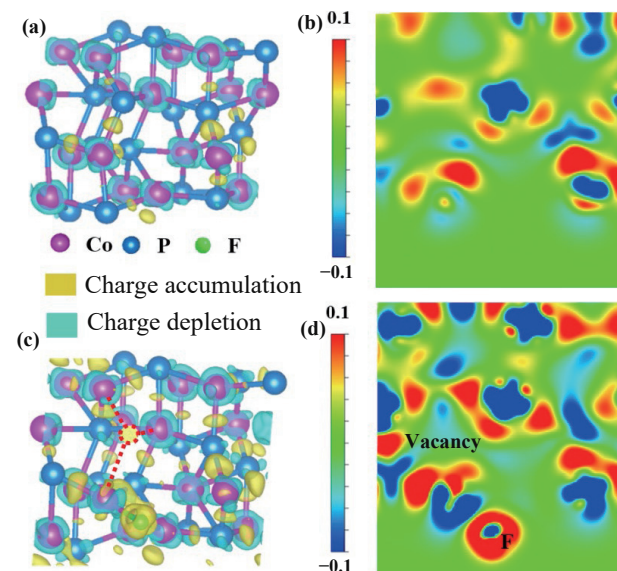


**Figure 7** (a) and (c) Charge difference distribution and (b) and (d) corresponding map of electronic location function (ELF) of CoP/CF and F-CoP/CF, the electron probability distribution varies from  $-0.1$  (blue color) to  $0.1$  (red color).

In addition, 3D Cu foam with high electronic conductivity would lead to the fast electrons flow in electrode. And 3D Cu foam as the framework material could provide a large number of nucleation sites for the active materials, which could prevent them agglomeration during growth, increasing the effective active sites.

Given the excellent OER and HER performance, to further demonstrate the potential for practical applications, an alkaline electrolyzer using 1 M KOH as electrolyte and F-CoP NAs/CF as both anode and cathode was assembled. The gas bubbles released from the anodes and cathodes are easily observed, as shown in Fig. 8(a), indicating an effective gas evolution reaction on both electrodes. The F-CoP NAs/CF||F-CoP NAs/CF cell achieves a current density of  $10$  mA·cm<sup>-2</sup> at the voltage of  $1.48$  V, which is much lower than Pt/C/CF||RuO<sub>2</sub>/CF ( $1.66$  V) (Fig. 8(b)), suggesting that the catalytic outputs of the electrolyzer assembled with our catalysts are better than that of Pt/C/CF||RuO<sub>2</sub>/CF, and which is also superior to those reported for recent state-of-the-art electrocatalysts shown in Fig. 8(d) and Table S5 in the ESM. In addition, the F-CoP/CF||F-CoP/CF electrolyzer can retain a stable

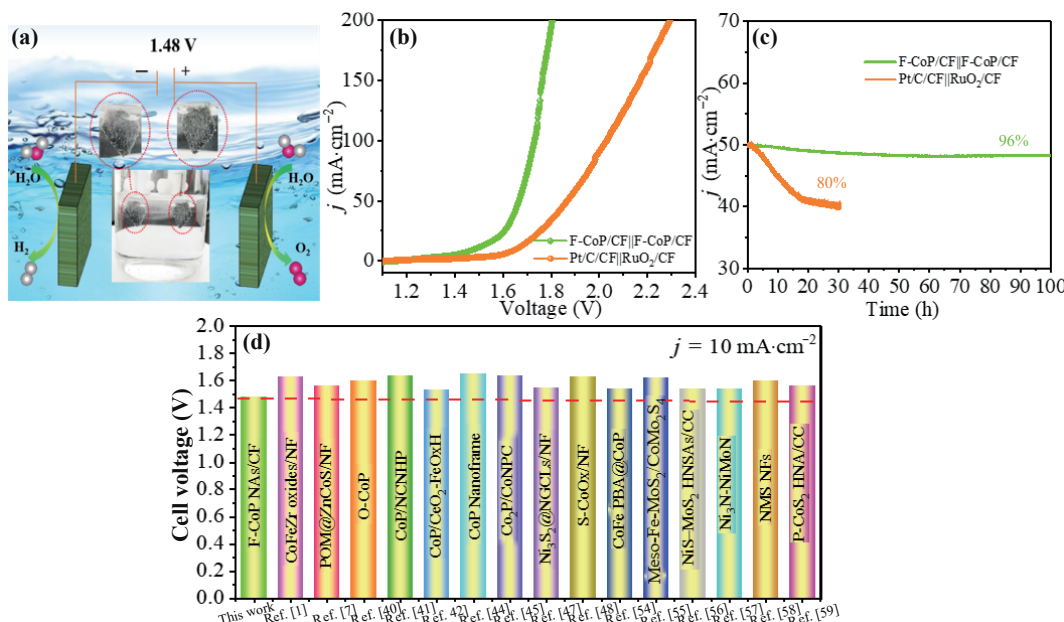


**Figure 8** (a) Schematic illustration of water splitting device. (b) Linear sweep voltammetry (LSV) curves of F-CoP/CF||F-CoP/CF and Pt/C/CF||RuO<sub>2</sub>/CF cells for overall water splitting. (c) The current density–time ( $i$ – $t$ ) curves of F-CoP/CF||F-CoP/CF and Pt/C/CF||RuO<sub>2</sub>/CF cells at the constant potential of 1.48 and 1.66 V for 100 h test, respectively. (d) Cell voltages of different electrolyzer constructed by bifunctional electrocatalysts for water electrolysis. The electrolyte is 1.0 M KOH.

cell voltage for over 100 h of continuous operation without obvious degradation at the constant potential of 1.48 V (Fig. 8(c)), which again demonstrates excellent long-term durability of our catalysts. To further verify the stability of F-CoP NAs/CF, the characterizations of SEM and XRD of the electrocatalyst after stability test were carried out. As we can see from the SEM image, the acicular nanoarrays morphology of the F-CoP is well preserved after stability test (Fig. S6(a) in the ESM). The XRD pattern of F-CoP NAs/CF after stability test does not appear new peak or shift of original peaks (Fig. S6(b) in the ESM), indicating that robust stability of F-CoP NAs/CF after stability test. The low cell voltage and long-term durability of F-CoP NAs/CF demonstrate their promising practical applications for efficient overall water splitting.

## 4 Conclusions

In summary, a simple, cost-efficient, and general fluorination method was developed to realize the surface reconstruction, F atom doping, and P vacancy of CoP nanoarrays, thus obtained the precious metal-free electrocatalysts with high overall water-splitting performance. F-CoP NAs/CF delivered an overpotential of only 35 mV at a current density of  $10 \text{ mA} \cdot \text{cm}^{-2}$  with a low Tafel slope of  $32 \text{ mV} \cdot \text{dec}^{-1}$  for HER, a small overpotential of 231 mV at  $50 \text{ mA} \cdot \text{cm}^{-2}$  with a Tafel slope of  $73.19 \text{ mV} \cdot \text{dec}^{-1}$  for OER, and the corresponding overall water-splitting electrolyzer requires a cell voltage of 1.48 V at  $10 \text{ mA} \cdot \text{cm}^{-2}$  in 1 M KOH, and the catalyst demonstrates excellent durability for 100 h continuous running. The excellent electrocatalytic performance can be mainly attributed to the increase of active sites induced by the surface reconstruction and the regulation of the charge distribution caused by F atom doping and P vacancy. This work not only proposed a generic and effective methodology to improve the overall water splitting performance through the synergistic effect of multiple regulatory engineering, but also opened a new avenue to design and construct various noble-metal-free electrocatalysts with an attracted prospect for practical applications.

## Acknowledgments

The work reported here was supported by the National Natural

Science Foundation of China (Nos. 52072196, 52002199, 52002200, and 52102106), Major Basic Research Program of Natural Science Foundation of Shandong Province (No. ZR2020ZD09), the Natural Science Foundation of Shandong Province (Nos. ZR2019BEM042 and ZR2020QE063), the Innovation and Technology Program of Shandong Province (No. 2020KJA004), and the Taishan Scholars Program of Shandong Province (No. ts201511034). We express our grateful thanks to them for their financial support. The authors want to thank Shiyanjia Lab for the support of DFT calculations.

**Electronic Supplementary Material:** Supplementary Material (additional SEM images of Co(OH)F/CF, SEM and TEM images of F-CoP NAs/CF-30 and F-CoP NAs/CF-90, the atomic percentage of F-CoP NAs/CF in XPS spectra, electrochemical details, relevant electrochemical test results and comparations, and the hydrogen adsorption free energy of CoP and F-CoP) is available in the online version of this article at <https://doi.org/10.1007/s12274-022-4702-y>.

## References

- [1] Li, R. Q.; Wan, X. Y.; Chen, B. L.; Cao, R. Y.; Ji, Q. H.; Deng, J.; Qu, K. G.; Wang, X. B.; Zhu, Y. C. Hierarchical Ni<sub>3</sub>N/Ni<sub>0.2</sub>Mo<sub>0.8</sub>N heterostructure nanorods arrays as efficient electrocatalysts for overall water and urea electrolysis. *Chem. Eng. J.* **2021**, *409*, 128240.
- [2] Huang, L. L.; Chen, D. W.; Luo, G.; Lu, Y. R.; Chen, C.; Zou, Y. Q.; Dong, C. L.; Li, Y. F.; Wang, S. Y. Zirconium-regulation-induced bifunctionality in 3D cobalt-iron oxide nanosheets for overall water splitting. *Adv. Mater.* **2019**, *31*, 1901439.
- [3] Feng, L. L.; Li, S. N.; He, D. Y.; Cao, L. Y.; Li, G. D.; Guo, P. H.; Huang, J. F. Heterostructured VN/Mo<sub>2</sub>C nanoparticles as highly efficient pH-universal electrocatalysts toward the hydrogen evolution reaction. *ACS Sustainable Chem. Eng.* **2021**, *9*, 15202–15211.
- [4] Wei, P.; Sun, X. P.; Wang, M. H.; Xu, J. H.; He, Z. M.; Li, X. G.; Cheng, F. Y.; Xu, Y.; Li, Q.; Han, J. T. et al. Construction of an N-decorated carbon-encapsulated W<sub>2</sub>C/WP heterostructure as an efficient electrocatalyst for hydrogen evolution in both alkaline and acidic media. *ACS Appl. Mater. Interfaces* **2021**, *13*, 53955–53964.
- [5] Bellani, S.; Antognazza, M. R.; Bonaccorso, F. Carbon-based

- photocathode materials for solar hydrogen production. *Adv. Mater.* **2019**, *31*, 1801446.
- [6] Zhou, Q. W.; Shen, Z. H.; Zhu, C.; Li, J. C.; Ding, Z. Y.; Wang, P.; Pan, F.; Zhang, Z. Y.; Ma, H. X.; Wang, S. Y. et al. Nitrogen-doped CoP electrocatalysts for coupled hydrogen evolution and sulfur generation with low energy consumption. *Adv. Mater.* **2018**, *30*, 1800140.
- [7] Gautam, J.; Liu, Y.; Gu, J.; Ma, Z. Y.; Zha, J. J.; Dahal, B.; Zhang, L. N.; Chishti, A. N.; Ni, L. B.; Diao, G. W. et al. Fabrication of polyoxometalate anchored zinc cobalt sulfide nanowires as a remarkable bifunctional electrocatalyst for overall water splitting. *Adv. Funct. Mater.* **2021**, *31*, 2106147.
- [8] Zhang, J. T.; Zhang, Z.; Ji, Y. F.; Yang, J. D.; Fan, K.; Ma, X. Z.; Wang, C.; Shu, R. Y.; Chen, Y. Surface engineering induced hierarchical porous  $\text{Ni}_1\text{P}_5\text{-Ni}_2\text{P}$  polymorphs catalyst for efficient wide pH hydrogen production. *Appl. Catal. B Environ.* **2021**, *282*, 119609.
- [9] Sun, J.; Du, L.; Sun, B. Y.; Han, G. K.; Ma, Y. L.; Wang, J. J.; Huo, H.; Du, C. Y.; Yin, G. P. Bifunctional  $\text{LaMn}_{0.3}\text{Co}_{0.7}\text{O}_3$  perovskite oxide catalyst for oxygen reduction and evolution reactions: The optimized  $e_g$  electronic structures by manganese dopant. *ACS Appl. Mater. Interfaces* **2020**, *12*, 24717–24725.
- [10] Kong, F. T.; Qiao, Y.; Zhang, C. Q.; Fan, X. H.; Kong, A. G.; Shan, Y. K. Unadulterated carbon as robust multifunctional electrocatalyst for overall water splitting and oxygen transformation. *Nano Res.* **2020**, *13*, 401–411.
- [11] Guan, H. M.; Li, W. T.; Han, J.; Yi, W. C.; Bai, H.; Kong, Q. H.; Xi, G. C. General molten-salt route to three-dimensional porous transition metal nitrides as sensitive and stable Raman substrates. *Nat Commun.* **2021**, *12*, 1376.
- [12] Qu, G. X.; Wu, T. L.; Yu, Y. N.; Wang, Z. K.; Zhou, Y.; Tang, Z. D.; Yue, Q. Rational design of phosphorus-doped cobalt sulfides electrocatalysts for hydrogen evolution. *Nano Res.* **2019**, *12*, 2960–2965.
- [13] Lin, C.; Wang, P. Y.; Jin, H. H.; Zhao, J. H.; Chen, D.; Liu, S. L.; Zhang, C. T.; Mu, S. C. An iron-doped cobalt phosphide nano-electrocatalyst derived from a metal-organic framework for efficient water splitting. *Dalton Trans.* **2019**, *48*, 16555–16561.
- [14] Xu, Q. C.; Jiang, H.; Li, Y. H.; Liang, D.; Hu, Y. J.; Li, C. Z. *In-situ* enriching active sites on co-doped Fe-Co4N@N-C nanosheet array as air cathode for flexible rechargeable Zn-air batteries. *Appl. Catal. B Environ.* **2019**, *256*, 117893.
- [15] Ye, Z. Q.; Jiang, Y.; Li, L.; Wu, F.; Chen, R. J. A high-efficiency CoSe electrocatalyst with hierarchical porous polyhedron nanoarchitecture for accelerating polysulfides conversion in Li-S batteries. *Adv. Mater.* **2020**, *32*, 2002168.
- [16] Xu, Q. C.; Jiang, H.; Duan, X. Z.; Jiang, Z.; Hu, Y. J.; Boettcher, S. W.; Zhang, W. Y.; Guo, S. J.; Li, C. Z. Fluorination-enabled reconstruction of NiFe electrocatalysts for efficient water oxidation. *Nano Lett.* **2021**, *21*, 492–499.
- [17] Zhang, G. W.; Wang, B.; Bi, J. L.; Fang, D. Q.; Yang, S. C. Constructing ultrathin CoP nanomeshes by Er-doping for highly efficient bifunctional electrocatalysts for overall water splitting. *J. Mater. Chem. A* **2019**, *7*, 5769–5778.
- [18] Pan, Y.; Sun, K. A.; Lin, Y.; Cao, X.; Cheng, Y. S.; Liu, S. J.; Zeng, L. Y.; Cheong, W. C.; Zhao, D.; Wu, K. L. et al. Electronic structure and d-band center control engineering over M-doped CoP (M = Ni, Mn, Fe) hollow polyhedron frames for boosting hydrogen production. *Nano Energy* **2019**, *56*, 411–419.
- [19] Xiong, B. Y.; Chen, L. S.; Shi, J. L. Anion-containing noble-metal-free bifunctional electrocatalysts for overall water splitting. *ACS Catal.* **2018**, *8*, 3688–3707.
- [20] Lu, X. Y.; Yim, W. L.; Suryanto, B. H.; R.; Zhao, C. Electrocatalytic oxygen evolution at surface-oxidized multiwall carbon nanotubes. *J. Am. Chem. Soc.* **2015**, *137*, 2901–2907.
- [21] Pande, S.; Huang, W.; Shao, N.; Wang, L. M.; Khetrapal, N.; Mei, W. N.; Jian, T.; Wang, L. S.; Zeng, X. C. Structural evolution of core-shell gold nanoclusters:  $\text{Au}_n$  ( $n = 42\text{--}50$ ). *ACS Nano* **2016**, *10*, 10013–10022.
- [22] Liu, Z. H.; Tan, H.; Xin, J. P.; Duan, J. Z.; Su, X. W.; Hao, P.; Xie, J. F.; Zhan, J.; Zhang, J.; Wang, J. J. et al. Metallic intermediate phase inducing morphological transformation in thermal nitridation:  $\text{Ni}_3\text{FeN}$ -based three-dimensional hierarchical electrocatalyst for water splitting. *ACS Appl. Mater. Interfaces* **2018**, *10*, 3699–3706.
- [23] Xu, T. T.; Yang, L.; Li, J.; Usoltseva, N.; An, V.; Jin, X.; Zhang, C.; Zhang, X. L.; Liu, B. D.  $\text{NH}_4\text{F}$ -induced morphology control of CoP nanostructures to enhance the hydrogen evolution reaction. *Inorg. Chem.* **2021**, *60*, 10781–10790.
- [24] Sun, Y. K.; Liu, T.; Li, Z. J.; Meng, A. L.; Li, G. C.; Wang, L.; Li, S. X. Morphology and interfacial charge regulation strategies constructing 3D flower-like  $\text{Co@CoP}_2$  heterostructure electrocatalyst for efficient overall water splitting. *Chem. Eng. J.* **2022**, *433*, 133684.
- [25] Zha, M.; Pei, C. G.; Wang, Q.; Hu, G. Z.; Feng, L. G. Electrochemical oxygen evolution reaction efficiently boosted by selective fluoridation of  $\text{FeNi}_3$  alloy/oxide hybrid. *J. Energy Chem.* **2020**, *47*, 166–171.
- [26] Wang, Q. Q.; Li, J. Q.; Li, Y. J.; Shao, G. M.; Jia, Z.; Shen, B. L. Non-noble metal-based amorphous high-entropy oxides as efficient and reliable electrocatalysts for oxygen evolution reaction. *Nano Res.*, in press, <https://doi.org/10.1007/s12274-022-4179-8>.
- [27] Li, M.; Wang, S. L.; Wang, X. Z.; Tian, X. L.; Wu, X.; Zhou, Y. T.; Hua, G. Z.; Feng, L. G. Structure evolution from  $\text{Fe}_2\text{Ni}$  MIL MOF to carbon confined O-doped  $\text{FeNi}/\text{FeF}_2$  via partial fluorination for improved oxygen evolution reaction. *Chem. Eng. J.* **2022**, *442*, 136165.
- [28] Liu, Z.; Liu, H.; Gu, X. C.; Feng, L. G. Oxygen evolution reaction efficiently catalyzed by a quasi-single-crystalline cobalt fluoride. *Chem. Eng. J.* **2020**, *397*, 125500.
- [29] Anjum, M. A. R.; Okyay, M. S.; Kim, M.; Lee, M. H.; Park, N.; Lee, J. S. Bifunctional sulfur-doped cobalt phosphide electrocatalyst outperforms all-noble-metal electrocatalysts in alkaline electrolyzer for overall water splitting. *Nano Energy* **2018**, *53*, 286–295.
- [30] Men, Y. N.; Li, P.; Yang, F. L.; Cheng, G. Z.; Chen, S. L.; Luo, W. Nitrogen-doped CoP as robust electrocatalyst for high-efficiency pH-universal hydrogen evolution reaction. *Appl. Catal. B Environ.* **2019**, *253*, 21–27.
- [31] Yan, D. F.; Li, Y. X.; Huo, J.; Chen, R.; Dai, L. M.; Wang, S. Y. Defect chemistry of nonprecious-metal electrocatalysts for oxygen reactions. *Adv. Mater.* **2017**, *29*, 1606459.
- [32] He, Q.; Wan, Y. Y.; Jiang, H. L.; Pan, Z. W.; Wu, C. Q.; Wang, M.; Wu, X. J.; Ye, B. J.; Ajayan, P. M.; Song, L. Nickel vacancies boost reconstruction in nickel hydroxide electrocatalyst. *ACS Energy Lett.* **2018**, *3*, 1373–1380.
- [33] Zhou, X. C.; Gao, H.; Wang, Y. F.; Liu, Z.; Lin, J. Q.; Ding, Y. P. Vacancies-enriched 3D hierarchical reduced cobalt phosphide as a precursor template for defect engineering for efficient water oxidation. *J. Mater. Chem. A* **2018**, *6*, 14939–14948.
- [34] Kresse, G.; Joubert, D. From ultrasoft pseudopotentials to the projector augmented-wave method. *Phys. Rev. B* **1999**, *59*, 1758–1775.
- [35] Perdew, J. P.; Burke, K.; Ernzerhof, M. Generalized gradient approximation made simple. *Phys. Rev. Lett.* **1996**, *77*, 3865–3868.
- [36] Xu, K.; Sun, Y. Q.; Li, X. L.; Zhao, Z. H.; Zhang, Y. Q.; Li, C. C.; Fan, H. J. Fluorine-induced dual defects in cobalt phosphide nanosheets enhance hydrogen evolution reaction activity. *ACS Materials Lett.* **2020**, *2*, 736–743.
- [37] Yuan, G. J.; Bai, J. L.; Zhang, L.; Chen, X.; Ren, L. L. The effect of P vacancies on the activity of cobalt phosphide nanorods as oxygen evolution electrocatalyst in alkali. *Appl. Catal. B Environ.* **2021**, *284*, 119693.
- [38] Xu, J. Y.; Liu, T. F.; Li, J. J.; Li, B.; Liu, Y. F.; Zhang, B. S.; Xiong, D. H.; Amorim, I.; Li, W.; Liu, L. F. Boosting the hydrogen evolution performance of ruthenium clusters through synergistic coupling with cobalt phosphide. *Energy Environ. Sci.* **2018**, *11*, 1819–1827.
- [39] Wu, Y. T.; Wang, H.; Ji, S.; Pollet, B. G.; Wang, X. Y.; Wang, R. F. Engineered porous  $\text{Ni}_2\text{P}$ -nanoparticle/ $\text{Ni}_2\text{P}$ -nanosheet arrays via the Kirkendall effect and Ostwald ripening towards efficient overall water splitting. *Nano Res.* **2020**, *13*, 2098–2105.

- [40] Zhou, G. Y.; Li, M.; Li, Y. L.; Dong, H.; Sun, D. M.; Liu, X. E.; Xu, L.; Tian, Z. Q.; Tang, Y. W. Regulating the electronic structure of CoP nanosheets by O incorporation for high-efficiency electrochemical overall water splitting. *Adv. Funct. Mater.* **2020**, *30*, 1905252.
- [41] Pan, Y.; Sun, K. A.; Liu, S. J.; Cao, X.; Wu, K. L.; Cheong, W. C.; Chen, Z.; Wang, Y.; Li, Y.; Liu, Y. Q. et al. Core–shell ZIF-8@ZIF-67-derived CoP nanoparticle-embedded N-doped carbon nanotube hollow polyhedron for efficient overall water splitting. *J. Am. Chem. Soc.* **2018**, *140*, 2610–2618.
- [42] Tan, Y.; Che, Q. J.; Li, Q. Constructing double-layer CoP/CeO<sub>2</sub>-FeO<sub>x</sub>H hybrid catalysts for alkaline and neutral water splitting. *ACS Sustainable Chem. Eng.* **2021**, *9*, 11981–11990.
- [43] Liu, Z.; Yu, X.; Xue, H. G.; Feng, L. G. A nitrogen-doped CoP nanoarray over 3D porous Co foam as an efficient bifunctional electrocatalyst for overall water splitting. *J. Mater. Chem. A* **2019**, *7*, 13242–13248.
- [44] Ji, L. L.; Wang, J. Y.; Teng, X.; Meyer, T. J.; Chen, Z. F. CoP nanoframes as bifunctional electrocatalysts for efficient overall water splitting. *ACS Catal.* **2020**, *10*, 412–419.
- [45] Liu, H. T.; Guan, J. Y.; Yang, S. X.; Yu, Y. H.; Shao, R.; Zhang, Z. P.; Dou, M. L.; Wang, F.; Xu, Q. Metal-organic framework-derived Co<sub>2</sub>P nanoparticle/multi-doped porous carbon as a trifunctional electrocatalyst. *Adv Mater.* **2020**, *32*, 2003649.
- [46] Fang, H. Y.; Huang, T. Z.; Sun, Y.; Kang, B. T.; Liang, D.; Yao, S.; Yu, J. M.; Dinesh, M. M.; Wu, S.; Lee, J. Y. et al. Metal-organic framework-derived core–shell-structured nitrogen-doped CoC<sub>x</sub>/FeCo@C hybrid supported by reduced graphene oxide sheets as high performance bifunctional electrocatalysts for ORR and OER. *J Catal.* **2019**, *371*, 185–195.
- [47] Li, B. L.; Li, Z. S.; Pang, Q.; Zhang, J. Z. Core/shell cable-like Ni<sub>3</sub>S<sub>2</sub> nanowires/N-doped graphene-like carbon layers as composite electrocatalyst for overall electrocatalytic water splitting. *Chem. Eng. J.* **2020**, *401*, 126045.
- [48] Yu, X. X.; Yu, Z. Y.; Zhang, X. L.; Li, P.; Sun, B.; Gao, X. C.; Yan, K.; Liu, H.; Duan, Y.; Gao, M. R. et al. Highly disordered cobalt oxide nanostructure induced by sulfur incorporation for efficient overall water splitting. *Nano Energy* **2020**, *71*, 104652.
- [49] Ouyang, Y. X.; Ling, C. Y.; Chen, Q.; Wang, Z. L.; Shi, L.; Wang, J. L. Activating inert basal planes of MoS<sub>2</sub> for hydrogen evolution reaction through the formation of different intrinsic defects. *Chem. Mater.* **2016**, *28*, 4390–4396.
- [50] Hammer, B.; Nørskov, J. K. Theoretical surface science and catalysis—calculations and concepts. *Adv. Catal.* **2000**, *45*, 71–129.
- [51] Chang, Y.; Cheng, Y.; Feng, Y. L.; Li, K.; Jian, H.; Zhang, H. Y. Upshift of the d band center toward the fermi level for promoting silver ion release, bacteria inactivation, and wound healing of alloy silver nanoparticles. *ACS Appl. Mater. Interfaces* **2019**, *11*, 12224–12231.
- [52] Su, L. X.; Gong, D.; Yao, N.; Li, Y. B.; Li, Z.; Luo, W. Modification of the intermediate binding energies on Ni/Ni<sub>3</sub>N heterostructure for enhanced alkaline hydrogen oxidation reaction. *Adv. Funct. Mater.* **2021**, *31*, 2106156.
- [53] Cheng, Y. C.; Fan, X.; Liao, F.; Lu, S. K.; Li, Y. Y.; Liu, L. B.; Li, Y. Q.; Lin, H. P.; Shao, M. W.; Lee, S. T. Os/Si nanocomposites as excellent hydrogen evolution electrocatalysts with thermodynamically more favorable hydrogen adsorption free energy than platinum. *Nano Energy* **2017**, *39*, 284–290.
- [54] Quan, L.; Li, S. H.; Zhao, Z. P.; Liu, J. Q.; Ran, Y.; Cui, J. Y.; Lin, W.; Yu, X. L.; Wang, L.; Zhang, Y. H. et al. Hierarchically assembling CoFe prussian blue analogue nanocubes on CoP nanosheets as highly efficient electrocatalysts for overall water splitting. *Small Methods* **2021**, *5*, 2100125.
- [55] Guo, Y. N.; Tang, J.; Henzie, J.; Jiang, B.; Xia, W.; Chen, T.; Bando, Y.; Kang, Y. M.; Hossain, M. S. A.; Sugahara, Y. et al. Mesoporous iron-doped MoS<sub>2</sub>/CoMo<sub>2</sub>S<sub>4</sub> heterostructures through organic-metal cooperative interactions on spherical micelles for electrochemical water splitting. *ACS Nano* **2020**, *14*, 4141–4152.
- [56] Guan, S. D.; Fu, X. L.; Lao, Z. Z.; Jin, C. H.; Peng, Z. J. NiS-MoS<sub>2</sub> heter-nanosheet array electrocatalysts for efficient overall water splitting. *Sustain. Energy Fuels* **2019**, *3*, 2056–2066.
- [57] Wu, A. P.; Xie, Y.; Ma, H.; Tian, C. G.; Gu, Y.; Yan, H. J.; Zhang, X. M.; Yang, G. Y.; Fu, H. G. Integrating the active OER and HER components as the heterostructures for the efficient overall water splitting. *Nano Energy* **2018**, *44*, 353–363.
- [58] Qian, Y. T.; Yu, J. M.; Zhang, Y.; Zhang, F. F.; Kang, Y. B.; Su, C. L.; Shi, H.; Kang, D. J.; Pang, H. Interfacial microenvironment modulation enhancing catalytic kinetics of binary metal sulfides heterostructures for advanced water splitting electrocatalysts. *Small Methods* **2022**, *6*, 2101186.
- [59] Li, Y. J.; Mao, Z. F.; Wang, Q.; Li, D. B.; Wang, R.; He, B. B.; Gong, Y. S.; Wang, H. W. Hollow nanosheet array of phosphorus-anion-decorated cobalt disulfide as an efficient electrocatalyst for overall water splitting. *Chem. Eng. J.* **2020**, *390*, 124556.